processes

MDPI

Article

Study on CO_2 Migration–Dissolution Characteristics in Saline Aquifers Under the Influence of Discontinuous Lenticular Shale Layers

Bohao Wu [1], Yuming Tao [1], Jiubo Yang [1], Jihao Sun [1], Ying Bi [2], Kaixuan Feng [3], Chao Chang [1,*] and Shaohua Li [3,*]

[1] College of Marine Engineering, Dalian Maritime University, Dalian 116026, China; bhw@dlmu.edu.cn (B.W.)
[2] School of Science & Engineering, Tulane University, New Orleans, LA 70118-5698, USA
[3] Key Laboratory of Ocean Energy Utilization and Energy Conservation of the Ministry of Education, School of Energy and Power Engineering, Dalian University of Technology, Dalian 116024, China
* Correspondence: chaochang@dlmu.edu.cn (C.C.); shaolee20@mail.dlut.edu.cn (S.L.)

Abstract

During CO_2 storage in deep saline aquifers, low-permeability lenticular shale layers alter CO_2 migration and affect dissolution trapping, but their impacts remain unclear. In this study, a two-dimensional radial numerical model coupling gas–brine two-phase flow and mass transfer is developed to simulate CO_2 plume evolution and dissolution beneath discontinuous lenticular shale layers. In the model, lenticular shale interlayers are represented as discontinuous low-permeability barriers, and their geometry is characterized by radial length and vertical thickness. The blocking effect of lenticular shale layers induces bypass flow, promotes lateral plume spreading, and prolongs contact time between CO_2 and brine, which increases dissolution during 250 to 1000 days of injection. When the permeability anisotropy ratio is 0.001, upward migration of CO_2 is suppressed and a high-concentration retention zone forms beneath the lenticular shale layer. As the radial length of the lenticular shale layers increases from 150 to 250 m, the plume expands and the bypass-flow path lengthens, which strengthens lateral CO_2 spreading and redistributes dissolved CO_2 concentration. In contrast, varying the thickness of the lenticular shale layers from 6 to 10 m has a relatively limited influence on the extent of bypass flow and the morphology of the concentration field.

Keywords: multiphase flow; porous media; CO_2 geological storage; dissolution trapping; lenticular body; heterogeneity

Check for updates

Academic Editor: Youguo Yan

Received: 13 February 2026
Revised: 14 March 2026
Accepted: 15 March 2026
Published: 24 March 2026

Copyright: © 2026 by the authors. Licensee MDPI, Basel, Switzerland. This article is an open access article distributed under the terms and conditions of the Creative Commons Attribution (CC BY) license.

1. Introduction

In recent years, the large-scale emission of greenhouse gases, especially CO_2, has intensified global climate change and threatens the sustainable development of human society [1]. Carbon Capture, Utilization, and Storage (CCUS) is a key technology for achieving deep decarbonization and is studied in both research and policy contexts worldwide [2]. CO_2 geological storage is a core component of CCUS technology, utilizing geological formations such as depleted oil and gas reservoirs or deep saline aquifers to store the captured CO_2 [3]. These geological settings are generally evaluated in terms of storage capacity, injectivity, containment, and geomechanical integrity, which together determine their suitability for long-term CO_2 storage [4,5]. During CO_2 storage, complex physical and chemical interactions occur between the injected supercritical CO_2 and the saline aquifer, and secondary

trapping mechanisms, particularly dissolution trapping, can enhance long-term storage security by immobilizing CO_2 and reducing buoyant migration [6].

Despite the vast potential of geological storage, practical engineering faces challenges due to complex geological conditions. Previous studies often simplified the numerical simulations by assuming that the reservoir was homogeneous or had a simple layered structure [7–9]. Among these, sedimentological heterogeneity and stratigraphic baffling within sandstone reservoirs may create local low-permeability barriers that influence CO_2 migration pathways and retention behavior [10,11]. Unlike continuous caprocks, intra-reservoir discontinuous lenticular shale layers act as local baffles rather than complete seals and delay vertical migration by redirecting flow pathways [12].

Previous studies have examined how intra-reservoir shale barriers and layered heterogeneity influence CO_2 migration and dissolution [13]. Hansen et al. [14] showed through large-scale numerical simulations that permeability heterogeneity and background flow can substantially alter supercritical CO_2 dissolution behavior in the deep subsurface. Fang et al. [15] found that in randomly multilayered heterogeneous formations, gravity segregation and permeability variability jointly control plume migration and dissolution efficiency. In formations with strong vertical permeability contrast, CO_2 tends to migrate laterally along high-permeability layers, which suppresses vertical plume rise but can enhance dissolution efficiency [16]. Cavanagh and Haszeldine [17] showed that plume geometry in the Sleipner storage formation is controlled by thin intra-formational shale barriers, underscoring the role of internal low-permeability layers in delaying vertical migration and redistributing lateral flow. Reservoir-scale studies of discontinuous shale barrier systems further indicate that barrier continuity and abundance strongly control plume geometry and pressure buildup, with longer or more laterally continuous barriers tending to suppress vertical migration and promote lateral spreading [12]. Local blockage by intra-reservoir barriers may also enhance pressure buildup, which should be considered when evaluating safe injection conditions. In addition, site-screening studies have shown that sedimentological heterogeneity and stratigraphic baffling potential are important considerations in evaluating CO_2 migration behavior and storage-site performance [11].

CO_2 migration and dissolution in deep saline aquifers are governed by buoyancy-driven upward rise and pressure-gradient-driven radial spreading. Reservoir heterogeneity reshapes the two-phase front and interfacial area, and it redistributes the plume by changing the pathways of pressure propagation [18]. In layered reservoirs with strong contrast, permeability differences produce distinct plume spreading fronts and shift both plume footprint and dissolved fraction. Field observations and interpretations show that thin intra-reservoir shale barriers split CO_2 into stacked layers and delay bulk upward migration [17]. They also promote lateral spreading within individual units and allow bypass into overlying strata through barrier terminations or weakly connected zones [19]. When the barriers are discontinuous, local blockage forces CO_2 to follow more tortuous paths. This process creates uneven pressure gradients and localized pressure focusing above and below the barriers, which alters far-field pressure dissipation and vertical pressure connectivity [20]. Mechanistic models further show that cross-layer flux and filling sequence depend on barrier properties and injection velocity, so shale geometry and petrophysical contrast affect pressure response and plume channeling in a measurable way [21].

Beyond permeability contrast, capillary and structural heterogeneity associated with discontinuous low-permeability interlayers such as lenticular shale layers redirect CO_2 migration and modify plume-scale spreading under buoyancy-dominated conditions [22]. Reservoir-scale simulations in randomly multilayered formations have shown that structural heterogeneity reorganizes plume footprint by guiding CO_2 along preferential layers, which changes the spatial distribution of free-phase CO_2 and the regions available for

dissolution [15]. Structural heterogeneity influences dissolution not only through plume shape but also through the timing of contact with fresh brine, because lateral spreading and slower post-injection migration can increase gas–brine contact area and residence time [23]. Existing studies have often examined plume redistribution in layered media separately from quantitative analyses of CO_2 dissolution in heterogeneous reservoirs, rather than assessing how both processes interact within the same structural setting [24]. Fewer studies have quantified how the longer bypass path and pressure redistribution produced by discontinuous lenticular shale interlayers modify CO_2-brine contact under radial injection, and how these changes affect dissolution trapping efficiency [18,22]. Against this background, the present study focuses on the coupled control of lenticular shale interlayers on plume pathway, pressure field, and dissolution trapping.

Although recent studies have examined capillary heterogeneity, multilayer migration, and vertical CO_2 flow beneath shale barriers, fewer investigations have isolated the coupled effects of idealized discontinuous lenticular shale layers on plume migration, pressure response, and dissolution trapping in radial saline-aquifer models [22,25]. In this study, we construct a geological model that includes lenticular shale layers through numerical simulations to investigate the effects of lenticular shale layer geometry, reservoir permeability anisotropy, and injection velocity on CO_2 migration. We also establish a sequestration efficiency factor and a nonlinear multi-parameter power-law correlation model, providing guidance for site selection and injection-strategy optimization in engineering applications.

2. Theoretical Model

This study employs a two-phase flow and mass transfer coupling model to describe the migration and dissolution processes of supercritical CO_2 in brine, while considering the effects of reservoir rock structure heterogeneity. The model is based on the laws of mass conservation and Darcy's law and introduces a mass transfer equation to describe CO_2 dissolution and migration.

2.1. Governing Equations for the Two-Phase Flow Field

The flow fields of the CO_2 phase and the brine phase are governed by their respective mass conservation equations and the extended Darcy's law. For two-phase flow in porous media (CO_2 phase $i = g$ and brine phase $i = w$), the mass conservation equation is expressed as [26]:

$$\frac{\partial}{\partial t}(\varphi_p \rho_i s_i) + \nabla \cdot (\rho_i u_i) = Q_i \tag{1}$$

Here, φ_p is the porosity of the formation, ρ_w and ρ_g are the densities of brine and gas, s_w and s_g are the saturations of brine and gas, and u_w and u_g represent the Darcy fluxes of the wetting and non-wetting phases, respectively. The Darcy fluxes are determined by Darcy's law [27]:

$$u_i = -\frac{k_{ri}}{\mu_i} k(\nabla p_i - \rho_i g) \tag{2}$$

Here, k is the absolute permeability of the reservoir matrix (m^2), k_{ri} is the relative permeability of phase i, μ_i is the dynamic viscosity of phase i (Pa·s), P is the pressure of phase i (Pa), ρi is the density of phase i (kg·m^{-3}), and g is the gravitational acceleration vector (m·s^{-2}).

In the two-phase flow formulation, CO_2 and brine saturations satisfy the following relation:

$$s_g + s_w = 1 \tag{3}$$

The interaction between the two phases is described by capillary pressure P_c and relative permeability k_{ri}, where the pressure difference between the non-wetting phase and the wetting phase is the capillary pressure:

$$p_c(s_w) = p_{nw} - p_w \tag{4}$$

Here, P_{nw} is the pressure of the non-wetting phase, and P_w is the pressure of the wetting phase. To analyze the changes in gas-liquid phase saturations, this study introduces the Brooks and Corey model [28]:

$$p_c(s_w) = p_{ec} s_e^{-\frac{1}{\lambda}} \tag{5}$$

$$s_e = \frac{s_w - s_{rw}}{1 - s_{rg} - s_{rw}} \tag{6}$$

Here, S_e is the effective saturation, S_{rw} and S_{rg} are the residual saturations of the brine and gas phases, respectively, P_{ec} is the capillary entry pressure, and λ is the pore size distribution index [9].

All verification cases in this chapter follow the conventional model settings reported in the corresponding references. The geometries, boundary conditions, initial conditions, and key parameters are kept consistent with those of the benchmark studies. Because multiple validation cases are included, the full parameter set for each case is not repeated here. Instead, emphasis is placed on whether the present model reproduces the reference results under the same setup. All validation cases are solved within the same numerical framework as the main model to ensure a consistent basis for comparison.

To validate the capillary pressure-saturation submodel, the study uses Berea sandstone core data to simulate the process of CO_2 displacing brine [29]. The model boundary conditions are set as impermeable boundaries at the top and bottom, CO_2 injection on the left, and a far-field boundary on the right. The capillary pressure-brine saturation curve is obtained through simulation and compared with the experimental data fitting curve from Pini et al. [29].

As shown in Figure 1a, within the capillary pressure range from 0 to 30 kPa, the curve predicted by the model follows the trend of the fitted experimental curve reported by Pini et al. These results indicate that the adopted Brooks–Corey type capillary pressure model represents the relationship between saturation and capillary pressure in two-phase flow.

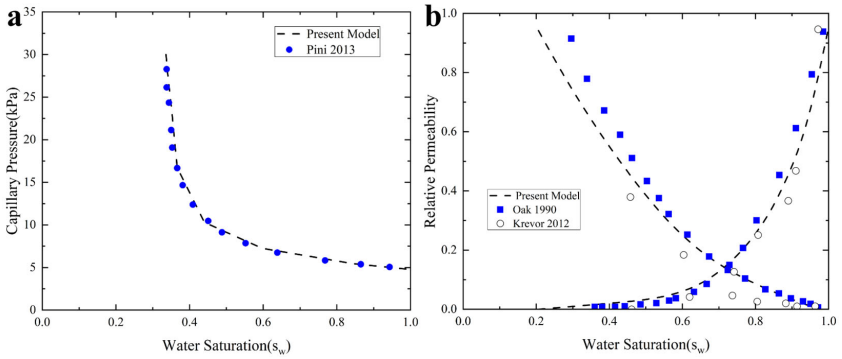


Figure 1. Comparison of the computational results of the model developed in this study with the experimental fitting results: (**a**) capillary pressure versus brine saturation compared with Pini et al. [29] and (**b**) relative permeability versus brine saturation compared with Oak et al. and Krevor et al. [30,31].

The relative permeability of the wetting phase is given by:

$$k_{rw} = s_e^{\left(\frac{2+3\lambda}{\lambda}\right)} \tag{7}$$

The relative permeability of the non-wetting phase is given by:

$$k_{rg} = (1 - s_e)^2 (1 - s_e^{\frac{2+\lambda}{\lambda}}) \tag{8}$$

After establishing the relative permeability model, typical relative permeability saturation data from the literature were selected as benchmarks to validate the model [30,31]. By calculating the relative permeability values at different saturations and comparing the simulation results with the experimental curves, the results show that the model's predictions are in good agreement with the experimental data. This validation demonstrates that the two-phase flow model is reliable and can serve as a foundation for constructing the coupled mass transfer model.

By combining the above conservation equations, we have:

$$\frac{\partial}{\partial t}\left(\varphi_p \sum_{i=1}^{N} \rho_i s_i\right) + \nabla \cdot \left(\sum_{i=1}^{N} \rho_i u_i\right) = \sum_{i=1}^{N} Q_i \tag{9}$$

The changes in thermophysical properties such as viscosity and density of supercritical CO_2 depend on temperature and pressure. This study uses equations applicable for a pressure range of 15 MPa to 40 MPa and a temperature range of 273 K to 553 K [32].

$$\rho_{co_2}(T, P) = 0.00036T^3 - 0.3693T^2 + 122T - 0.333P^2 + 32.54P - 12720 \tag{10}$$

$$\mu_{co_2}(T, P) = 7.14 \times 10^{-9}T^2 - 5.642 \times 10^{-6}T - 5.71 \times 10^{-9}P^2 + 2.186 \times 10^{-6}P + 0.0011 \tag{11}$$

To validate the accuracy of the overall two-phase flow displacement model, the simulation results were compared with the experimental data from Vivek et al. [8] and the analytical solution of the Buckley-Leverett model [33]. As shown in Figure 2, the numerical model captured the saturation profiles at different time scales, which were consistent with both the analytical solution of the Buckley-Leverett model and the simulation results from Vivek et al. [8]. The results confirm that the developed numerical model can reproduce the CO_2-brine displacement behavior across different scales.

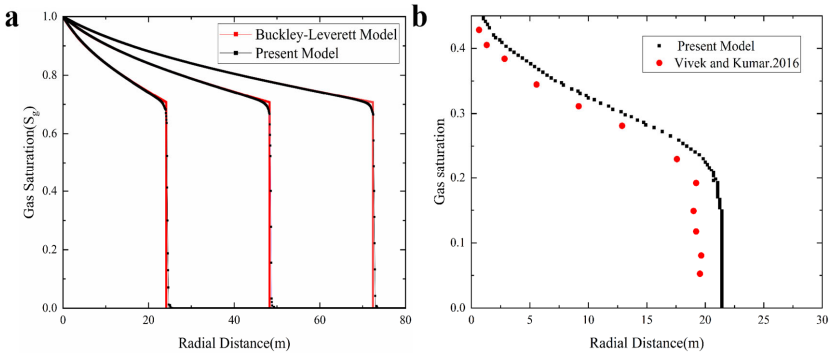


Figure 2. Verification of the gas saturation profiles of the present model: (**a**) vertical displacement profile compared with Buckley-Leverett analytical solution [33] and (**b**) radial displacement profile compared with results of Vivek et al. [8].

2.2. Mass-Transfer Model

In a multicomponent multiphase system, the migration of the dissolved phase in porous media is controlled by advection and diffusion. The advection-diffusion equation is

established based on the law of mass conservation. A transport model for dissolved CO_2 is used to describe the distribution and evolution of CO_2 in the liquid phase [34]:

$$\frac{\partial}{\partial t}\left(\varphi_p \rho_i S_i C_i^g\right) + \nabla \cdot \left(\rho_i u_i C_i^g\right) - \nabla \cdot \left(\varphi_p S_i D_i \nabla C_i^g \rho_i\right) = I_i^g \tag{12}$$

In the equation, ${C_g}^i$ is the mass fraction of the gas phase in phase i. D_i is the diffusion coefficient of the gas component in phase i, in units of $m^2 \cdot s^{-1}$, and is calculated using the Wilke-Chang equation while neglecting mechanical dispersion caused by velocity fluctuations. ${I_g}^i$ is the mass transfer rate of the gas component from the phase interface to phase i ($kg \cdot m^{-3} \cdot s^{-1}$) [34]. Because interfacial resistance controls mass transfer in soluble or slightly soluble systems, a non-equilibrium interphase mass transfer model is used to represent this behavior [35,36]. In this model, the mass transfer rate depends on the interphase mass transfer resistance, specific surface area, and the equilibrium concentration of the gas components, and is expressed by the following equation:

$$I_w^g = k_{n-w}^g a \rho_w (C_{ew}^g - C_w^g) = K_{n-w}^g \rho_w (C_{ew}^g - C_w^g) \tag{13}$$

Here, k_{n-w}^g represents the interphase mass transfer rate of the component, in units of m/s. a represents the interfacial specific surface area, in units of m^{-1}. ρ_w represents the density of the wetting phase, in units of $kg \cdot m^{-3}$. K_{n-w}^g is a constant known as the total interphase mass transfer rate, in units of s^{-1}. C_{ew}^g is the gas phase equilibrium concentration in the wetting phase, which refers to the concentration of the gas component in the liquid phase when it reaches equilibrium.

In this study, to facilitate the analysis and discussion of the subsequent results, CO_2 dissolution characteristics are represented in the form of normalized concentration. The normalized concentration is defined as the ratio of the dissolved CO_2 concentration predicted by the non-equilibrium mass transfer model to the equilibrium concentration in the liquid phase.

$$C_g = \frac{C_w^g}{C_{ew}^g} \tag{14}$$

To validate the accuracy of the mass transfer model, the simulation results were compared with the results from Ding et al. [9]. Figure 3 shows the trend of normalized CO_2 concentration along the radial profile with respect to reservoir length. The initial normalized CO_2 concentration is near 1, and it decreases to 0 as CO_2 migrates to about 1000 m, indicating limited dissolution into brine. The simulation results are consistent with the trend of the data from Ding et al., confirming the applicability of the constructed mass transfer model.

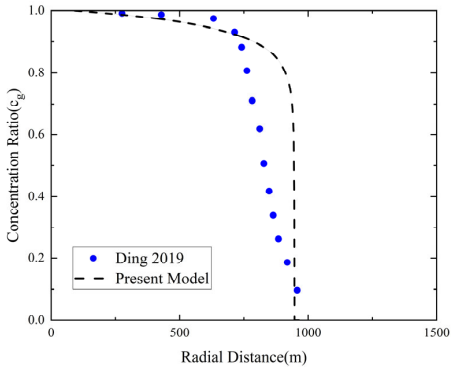


Figure 3. Comparison between the calculation results of this study's model and the simulation results of Ding et al. [9] showing the normalized CO_2 concentration versus radial distance.

3. Conceptual Model

3.1. Establishment of the Geometric Model

This study establishes a simplified two-dimensional radial model based on the geological background of the Shahejie Formation in the Bohai Bay Basin, China, to investigate the migration and dissolution behavior of supercritical CO_2 in saline aquifers [37]. The reservoirs of the Shahejie Formation in the Bohai Bay Basin often develop discontinuous mudstone lenticular shale layers, which exhibit certain heterogeneity characteristics [38].

To investigate the impact of lenticular shale layers on the CO_2 plume migration path and local capillary trapping, the reservoir is conceptualized as a sandstone system containing discontinuous lenticular shale layers. The geometric modeling adopts a simplified approach from mechanism-based models [39,40], where the lenticular shale layers are idealized as regular rectangular block obstacles, as shown in Figure 4. This geometric simplification is based on two considerations. First, representing the lenticular shale layers as regular geometric bodies avoids potential grid distortion and computational convergence issues that may arise from the real lens termination, while ensuring stable tracking of the multiphase flow interface. Second, regular geometry facilitates the parameterization of the radial length and spatial distribution of the shale layers, enabling the quantification of the impact of heterogeneity parameters on sequestration efficiency sensitivity. Although the model ignores the microscopic morphology of shale layer edges, it retains the barrier mechanism that drives bypassing and interlayer leakage under field conditions.

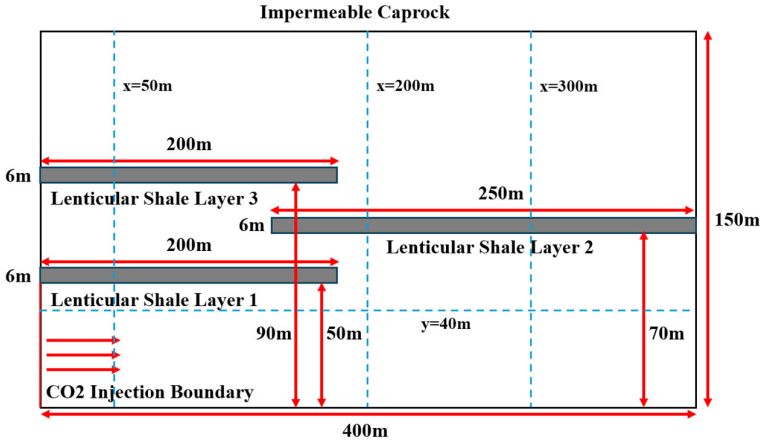


Figure 4. Schematic diagram of model geometry.

Furthermore, the 2D axisymmetric assumption presents certain limitations, as it essentially treats discrete lenticular bodies as continuous annular barriers. Under realistic 3D field conditions, the lateral gaps between complex discrete lenses would provide additional pathways for fluid bypass. Such 3D effects could lead to a more complex and asymmetric CO_2 plume shape, characterized by potential 3D viscous fingering and channeling phenomena [41]. Additionally, these extra lateral flow pathways would offer more dissipation routes for pressure, implying that local pressure buildup in 3D field scenarios may be weaker and pressure redistribution may be more diffuse than predicted by the current 2D model. Consequently, the 2D radial axisymmetric model also serves to provide a more stringent and conservative baseline scenario for evaluating local pressure buildup within the reservoir.

Reservoir parameters were taken from published studies for sensitivity analysis [42–46]. The target deep saline aquifer of the Shahejie Formation is located at an approximate depth of 1800 m, corresponding to an initial reservoir pressure of 18 MPa and a temperature of 323.15 K. The reservoir matrix is characterized as strongly water-wet tight sandstone, and

the formation fluid is modeled as saline brine with an initial density of 1020.7 kg·m^{-3}. CO_2 residual saturation was represented with the Brooks and Corey model and benchmarked against experimental saturation distributions for CO_2–brine systems to evaluate the two-phase flow model [28]. A CO_2 injection velocity was prescribed at the left boundary of the saline aquifer, with $u_{inj} = 0.4475 \times 10^{-6}$ m/s. The far-field right boundary was located 400 m from the injection well. The thickness of the lenticular shale layer was set to 6 m. Remaining property values are listed in Table 1.

Table 1. Main parameters of the model.

Temperature T/K	Pressure P/MPa	Brine Density ρ_w/kg·m^{-3}	Entry Capillary Pressure P_{ec}/kPa
323.15	18	1020.7	10
Reservoir Matrix Porosity φ_p	**Reservoir Matrix Permeability k/mD**	**Porosity of the Lenticular Shale layer φ_b**	**Lenticular Shale Layer Permeability k_b/mD**
0.25	50.65	0.1025	0.4865

This study defines the compressibility of CO_2 as a function of temperature and pressure to reflect its compressional behavior in the supercritical state, as shown in Equations (10) and (11). The formulation represents CO_2 compressibility as a function of temperature and pressure and captures the dynamic plume behavior in high-pressure reservoirs. The geochemical reactions between CO_2, minerals, and brine typically cause significant changes in pore structure and permeability over decades to centuries [47]. However, within the simulation time frame of this study, the impact of these chemical reactions is relatively small, and their effects on porosity and permeability can be neglected.

To simplify the calculations and maintain model stability, this study establishes the mathematical model based on the following assumptions:

(1) The brine is an incompressible fluid. This assumption is justified by the open constant-pressure boundary condition at x = 400 m, where $P = P_0$. Under this condition, substantial pressure buildup does not occur. Furthermore, our simulation results indicate that the maximum local volumetric compression rate induced by pressure perturbations is merely 0.06%. Such a minuscule volumetric strain is insufficient to fundamentally alter the multiphase flow displacement mechanisms.

(2) Under the low-velocity conditions considered, Darcy's law is applicable to two-phase flow of CO_2 and brine.

(3) The study focuses on the long-term migration and dissolution of the CO_2 plume, and no heat exchange is assumed between the fluid phases.

The numerical simulations were conducted using a finite-element framework, in which multiphase flow was governed by the Brooks–Corey model. For spatial discretization, an unstructured free triangular mesh was generated. To accurately capture the sharp multiphase interfaces and complex flow dynamics near the heterogeneous edges, a local mesh refinement strategy was implemented. The global maximum element size was set to 1.2 m, while grids along specific internal boundaries were refined to 0.2 m. The final model consists of 475,967 elements, ensuring high-resolution calculations independent of the grid. The mesh-independence of this discretization strategy was verified in our previous work [48]. To solve the highly coupled nonlinear governing equations, a combined numerical strategy was employed. A hybrid numerical solution strategy was adopted to ensure the accuracy and stability of the system. An iterative treatment was further employed to handle the strong convective and source terms. Together, these procedures improved computational efficiency.

3.2. Initial Conditions and Boundary Conditions

In the model developed in this study, the initial pressure and temperature conditions are shown in Equations (15) and (16). This initial temperature is used to determine the thermodynamic state of the model at t = 0 s, allowing the calculation of the initial density and viscosity of CO_2:

$$P(x, y, t)|_{t=0} = P_0 \tag{15}$$

$$T(x, y, t)|_{t=0} = T_0 \tag{16}$$

The thermo-hydraulic boundary condition at the left boundary and the pressure boundary at the right boundary are given by Equations (17) and (18).

$$u(x = 0, y, t) = u_{inj} \tag{17}$$

$$P(x = 400\ \text{m}, y, t) = P_0 \tag{18}$$

Under the isothermal assumption adopted in this study, both the aquifer and the injected CO_2 are assigned a uniform temperature of 323.15 K. This simplification is considered reasonable for the present model because the vertical extent of the computational domain is only 150 m, corresponding to a natural temperature variation of approximately 3.75–4.5 K under a typical geothermal gradient of 25–30 K/km. Previous studies have shown that plume migration is more sensitive to CO_2 density than to brine viscosity, because plume extent is primarily controlled by buoyancy [49]. Under the representative reservoir condition considered here, with a pressure of 18 MPa and a temperature of 323.15 K, such a limited temperature variation causes only minor changes in the thermophysical properties of CO_2, especially its density. As a result, it is not expected to alter the dominant trends in plume migration and dissolution identified in this study. In addition, the influence of temperature on CO_2 storage behavior has been reported to become more significant mainly under much larger temperature variations than those associated with the present model scale [50]. Nevertheless, for larger-scale reservoirs or strongly non-isothermal injection conditions, thermo-hydraulic coupling should be incorporated, and this will be considered in future work [51]. Regarding the mass transfer model boundary conditions, gas phase concentration or flux boundaries are specified at the gas–brine interface, while zero flux or fixed concentration conditions are applied at the outer boundary.

To quantify CO_2 storage potential in saline aquifers, we use a mass-based storage efficiency factor ϵ. Following the US DOE framework and related studies [52,53], this factor is defined as the ratio between the total mass of CO_2 stored in the reservoir at the end of injection and the theoretical maximum mass that the pore space can accommodate.

$$\epsilon = \frac{M_{injected}}{V_{pore} \cdot \rho_{CO_2,res}} \tag{19}$$

Here, $M_{injected}$ is the simulated total mass of stored CO_2 including gas and dissolved phases, V_{pore} is the total pore volume of the reservoir, and $\rho_{CO2,res}$ is a reference CO_2 density at the reservoir-average temperature and pressure. Because CO_2 storage in deep saline aquifers is jointly controlled by multiple geologic and engineering factors, no single parameter can adequately describe the evolution of storage efficiency. Therefore, a multi-parameter nonlinear power-law expression is further introduced as follows [48].

$$\epsilon = \kappa \cdot {u_{\text{inj}}}^{\alpha} \cdot W^{\beta} \cdot H^{\gamma} \cdot \Gamma^{\delta} \tag{20}$$

Here, κ is a scaling coefficient that represents intrinsic reservoir properties, W is the radial length of the lenticular shale layer, and H is the shale thickness. The exponents α, β,

Γ, and δ quantify the influence of injection velocity, shale radial length, shale thickness, and the permeability anisotropy ratio, respectively. The expression provides the basis for the quantitative comparison in Sections 4.4–4.6, while its regression-based correlation analysis is further presented in Section 4.7.

4. Results and Discussion

4.1. Temporal Evolution of Pressure in the Saline Aquifer

Figure 5 shows the spatial evolution of pore pressure distribution in the formation during continuous CO_2 injection from 250 to 1000 days. The high-pressure region is concentrated near the injection end in the lower-left corner of the model, and the low-pressure region lies in the far-field area in the upper-right corner. The pressure fields at different times show that, although injection continues from 250 to 1000 days, the spatial pattern and magnitude of pressure remain consistent. The pressure distribution suggests that pressure perturbations propagate faster than advective fluid migration and reach the model boundaries early. The system then approaches dynamic equilibrium, and the flow field remains near a quasistatic state. This provides a stable potential field for subsequent fluid displacement. Additionally, the vertical pressure distribution exhibits significant spatial heterogeneity. The pressure in the near-well region on the left shows a decreasing trend, transitioning from the high-pressure area at the bottom to the low-pressure area at the top, while an anomalous local pressure inversion occurs in the far-well area on the right.

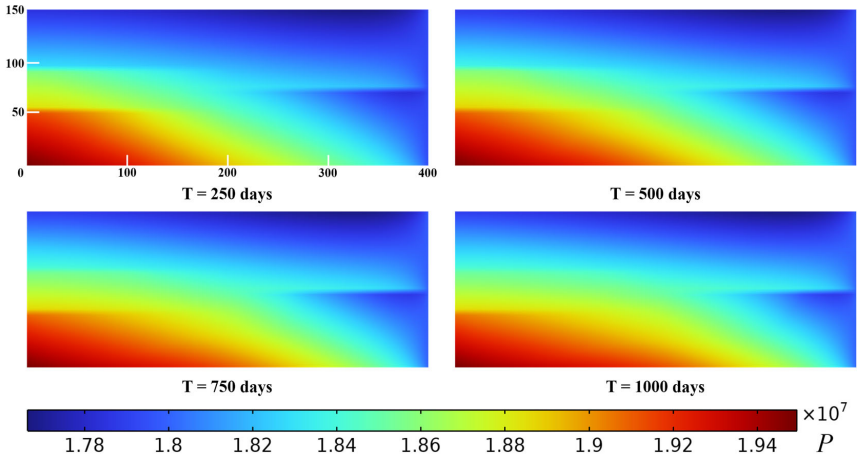


Figure 5. Temporal evolution of pore pressure distribution in the saline aquifers during continuous CO_2 injection from 250 to 1000 days.

To further quantify the pressure distribution patterns and gain deeper insight into the underlying flow mechanisms, this study selected radial cross-sections at a vertical distance of 40 m and vertical cross-sections at radial distances of 50 m and 300 m. The changes in pore pressure with distance were plotted at these locations to analyze the pressure response differences at various structural positions, as shown in Figure 6.

Figure 6a shows the evolution of pore pressure with radial distance and injection time in the lower injection area at a vertical distance of 40 m. The pressure decreases monotonically from the injection well toward the far-field boundary, creating a radial pressure gradient that drives fluid migration. In the near-well zone with radial distances from 0 to 200 m, the pressure response indicates a gradual decrease in pore pressure as injection time increases. This phenomenon is attributed to the improved flow behavior caused by the viscosity difference between the gas and brine phases in two-phase flow. Since the viscosity of supercritical CO_2 is lower than that of formation brine, the low-viscosity

gas plume expands radially in the near-well area and displaces the high-viscosity brine. Given that the flow resistance of the fluid is proportional to its viscosity, the expansion of the high-saturation gas phase region reduces the flow resistance in the near-well area. Under constant injection velocity, the driving pressure difference required to maintain flow decreases, leading to a gradual decline in pressure levels in the near-well area. Additionally, the pressure curves at different times converge at a radial distance of 200 m, corresponding to the geometric end of lenticular shale layer 1. Beyond 200 m, the fluid distribution remains dominated by brine, and the pressure wave propagates rapidly, establishing a quasi-steady state distribution of the flow field, causing the pressure curves in this region to overlap, with minimal time dependence.

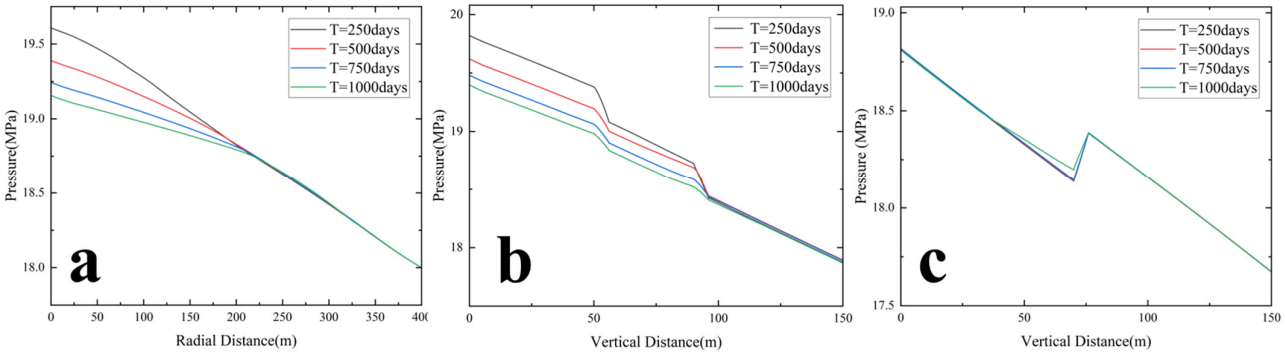


Figure 6. Reservoir pressure variation with radial and vertical distance at different injection times (250 to 1000 days): (**a**) radial cross section at a vertical distance of 40 m; (**b**) vertical cross section at a radial distance of 50 m; and (**c**) vertical cross section at a radial distance of 300 m.

Figure 6b shows the evolution of pore pressure with vertical distance and injection time in the near-well area at a radial distance of 50 m. Overall, the pressure curves exhibit a monotonically decreasing trend with increasing vertical height and its main gradient aligns with the hydrostatic pressure gradient of the formation fluid. Heterogeneity of the lithologic structure introduces local high-gradient features in the pressure curve. In the vertical distance intervals of 50 to 56 m and 90 to 96 m, corresponding to the lenticular shale layers 1 and 3, the absolute value of the slope increases to show steeper pressure drops. Low permeability reduces the efficiency of energy transfer in the pressure field across the lenticular shale layers. To maintain the continuity of potential energy across layers, large pressure gradients form within the layers to create local pressure drop zones.

Similar to the radial distribution, pressure curves at different times converge near a vertical distance of 96 m corresponding to the upper interface of lenticular shale layer 3. Below shale layer 3, the pressure curves remain distinct due to persistently high gas-phase saturation, which causes formation pressure to decline progressively with injection time, as low-viscosity CO_2 displaces brine to reduce flow resistance. Above shale layer 3, the four pressure curves overlap, which indicates that the gas-phase plume is trapped beneath the layer and has not broken through shale layer 3 on a large scale.

Figure 6c shows the evolution of pore pressure with vertical distance and injection time in the far-well area at a radial distance of 300 m. Unlike the characteristics in the near-well zone, the pressure distribution here exhibits time independence and spatial non-monotonicity. The pressure curves at different times overlap in the vertical distribution, which indicates that a stable gradient distribution of the pressure field has been established in the far-well area, unaffected by changes in the upstream gas-phase saturation. A local pressure spike occurs within the vertical distance range of 70 to 76 m, where the pressure above lenticular shale layer 2 is higher than the pressure below the layer. This phenomenon

results from the differences in the propagation of pressure waves through different flow paths.

In the near-well area, the upward diffusion of the pressure wave is blocked by lenticular shale layer 3, which causes the pressure energy to deflect and propagate radially. The confined space between lenticular shale layers 1 and 3 focuses and directs the pressure energy to create a local high-pressure zone above lenticular shale layer 2. Conversely, the area below shale layer 2 in the far-well region experiences pressure reduction due to geometric shielding by shale layer 1 and radial flow divergence, where the flow cross-section increases linearly with radial distance to maintain a lower pressure level. Shale layer 2 acts as a low-permeability medium connecting two different pressure systems and exhibits a linear transition of pressure from the lower interface to the upper interface, resulting in a pressure step in the curve.

4.2. Temporal Evolution of Gas-Phase Saturation in Saline Aquifers

Figure 7 shows the spatial distribution of gas-phase saturation during continuous CO_2 injection from day 250 to day 1000. CO_2 is less dense than brine. Injection pressure and buoyancy displace resident brine and produce simultaneous vertical migration and radial spreading. Lenticular shale layers constrain flow and generate a heterogeneous response. Early in the injection period, CO_2 accumulates beneath lenticular shale layer 1 within the basal brine aquifer, forming a high gas-saturation zone. The low-permeability and low-porosity shale acts as a capillary barrier that inhibits upward gas movement and redirects migration from vertical to lateral pathways.

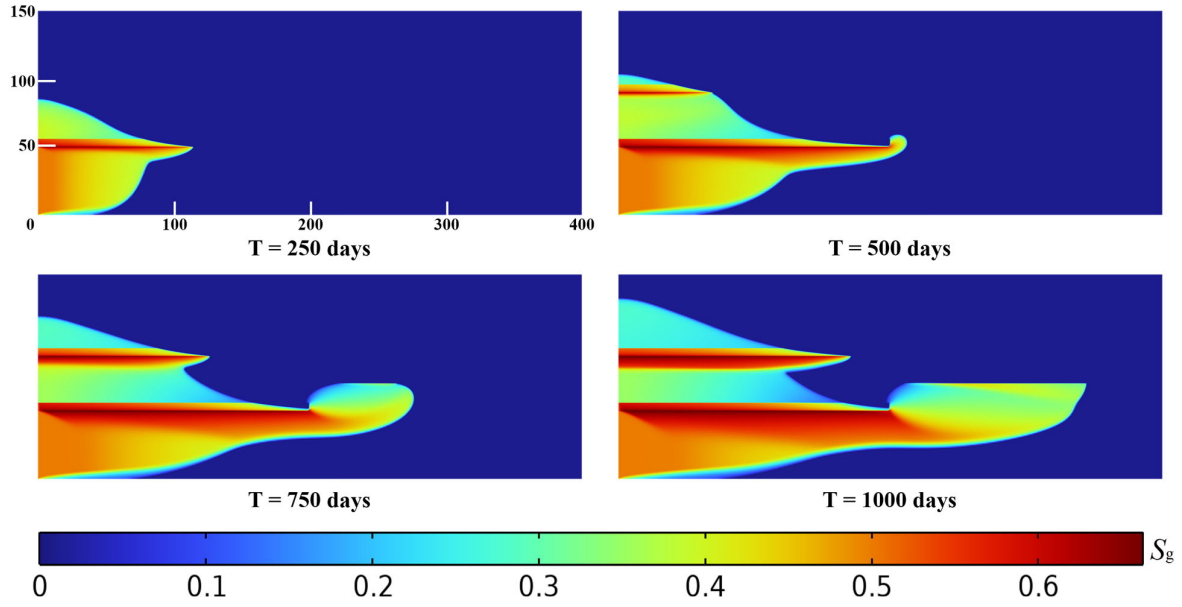


Figure 7. Temporal evolution of gas saturation in the saline aquifer during continuous CO_2 injection from 250 to 1000 days.

Over time, the CO_2 plume extends radially and enters the middle and upper saline aquifers through leakage across the shale matrix and bypass flow around shale edges. CO_2 accumulation exhibits pronounced spatial variability. Near the well, at the lower interface of lenticular shale layer 1, CO_2 accumulates rapidly and forms a high gas-saturation zone. At the distal location, at the lower interface of lenticular shale layer 2, saturation increases with time but remains below the near-well peak. This decline from left to right reflects two mechanisms. First, axisymmetric geometry increases flow cross-sectional area with radial distance. As the plume migrates outward, a fixed mass of CO_2 occupies a larger pore

volume, which lowers local gas-phase saturation. Second, the near-well shale forms a local trap. Only after the storage capacity beneath it approaches a saturation threshold does excess CO_2 spill laterally and supply the distal reservoir. This delayed supply produces a lagged increase in distal saturation.

To quantify radial spreading and post-barrier migration, we extracted one radial transect at a vertical distance of 40 m and two vertical transects at radial distances of 50 m and 200 m. Figure 8a shows gas-phase saturation along the basal injection interval at a vertical distance of 40 m as a function of radial distance and injection time. Gas-phase saturation remains high near the well indicating that brine has been displaced in this region. From day 250 to day 1000, the saturation front migrates outward and shows an abrupt drop consistent with an immiscible displacement front. The saturation profiles differ across injection stages. At day 250, limited injection time causes migration to be controlled by buoyancy and pressure gradients. CO_2 accumulates upward along the lower surface of lenticular shale layer 1, so a continuous high-saturation zone has not formed along the sampled transect, and near-well saturation is lower and decreases with radial distance. At day 1000, the profile shows a distinct saturation drop near the radial distance of 200 m, which differs from the trends at earlier times.

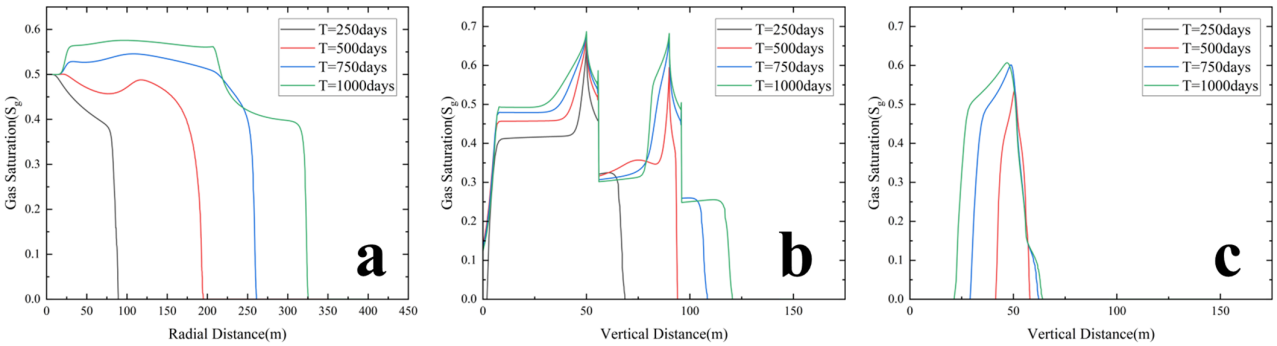


Figure 8. Variation of gas saturation with radial and vertical distance at different injection times (250 to 1000 days): (**a**) radial cross section at a vertical distance of 40 m; (**b**) vertical cross section at a radial distance of 50 m; and (**c**) vertical cross section at a radial distance of 200 m.

The right termination of lenticular shale layer 1 occurs at a radial distance of 200 m, which defines a transition in the migration pathway. Upstream of this point, between radial distances of 0 m and 200 m, the overlying lenticular shale confines CO_2 beneath the layer to promote a high gas-saturation accumulation zone. When the plume crosses the shale termination at 200 m, the constraint from the overlying shale is removed. Buoyancy diverts a large fraction of CO_2 upward around the shale edge into the overlying saline aquifers. This diversion reduces the lateral CO_2 flux along the basal saline aquifer, which lowers local gas-phase saturation and produces the pronounced drop in the profile.

Figure 8b shows gas-phase saturation in the near-well region at a radial distance of 50 m as a function of vertical position and injection time, which indicates that lithologic layering controls vertical distribution. The profiles show alternating peaks and troughs that align with the lithologic layering. Peaks occur at the base of each shale layer and the top of the underlying saline aquifer, while near-vertical drops coincide with shale tops, and troughs occur within the middle saline aquifer. Injected CO_2 migrates upward and accumulates beneath lenticular shale layer 1 to raise local pressure. Once this pressure exceeds the capillary entry pressure of the shale, CO_2 enters the low-permeability shale.

Saturation drops sharply at the upper interfaces of lenticular shale layers 1 and 3 to produce near-vertical decreases in the profiles. Although CO_2 enters the shale, the low permeability limits upward flux and causes CO_2 to remain within shale pores. When CO_2 reaches the overlying saline aquifer, buoyancy and pressure gradients redistribute the

fluid to prevent high saturation at the interface and produce a sharp drop. The gas then accumulates beneath the next shale layer and forms a new peak. These processes indicate that in the near-well high-pressure zone, shale layers do not fully block upward migration but act as high-saturation low-flux barriers.

Figure 8c shows gas-phase saturation in the distal region at a radial distance of 200 m as a function of vertical position and injection time. Unlike the layered accumulation near the well in Figure 8b, the profiles here show a single peak, with the maximum between vertical distances of 20 m and 60 m. In time, saturation remains zero at day 250, indicating that the CO_2 plume has not reached this location. Nonzero saturation appears after day 500. When CO_2 migrating along the basal aquifer reaches the termination of lenticular shale layer 1, buoyancy and pressure gradients drive upward leakage. The rising flow is then constrained by lenticular shale layer 2 on the right. The pressure field indicates a vertical pressure inversion across shale layer 2, with an upward adverse pressure gradient within the shale and at its interfaces. Gas becomes trapped beneath shale layer 2 and spreads laterally. Thickening of the gas layer promotes connection with upward spill flow supplied from below. As a result, saturation along this transect reflects the combined effects of upward spill supply from below and accumulation beneath the overlying shale. This process connects gas across the two stratigraphic levels and forms a continuous high-saturation zone, which produces the single-peak profile.

Figures 7 and 8 indicate that the staggered lenticular shale layers act analogously to baffles in process equipment. This discontinuous architecture allows upward migration of CO_2, but forces a tortuous pathway that includes lateral spreading, followed by bypass flow around the shale edge, and renewed spreading above. This mechanism lengthens the migration path and increases residence time to enhance sweeping of the upper portions of each saline aquifer. The resulting increase in contact area and contact time between CO_2 and brine promotes storage and improves macroscopic sweep efficiency.

4.3. Temporal Evolution of Dissolved CO_2 Distribution in a Saline Aquifer

Figure 9 shows the spatial distribution and evolution of normalized CO_2 concentration during continuous injection from day 250 to day 1000. The normalized CO_2 concentration distribution follows the gas saturation pattern, indicating enhanced dissolution beneath the lenticular shale layers. Acting as structural traps, these shale layers restrict upward CO_2 escape, confining the gas plume beneath the barriers and promoting lateral spreading along their bases. This accumulation increases CO_2-brine contact time and expands the interfacial area between gas and undersaturated brine. As the plume front migrates outward, CO_2 encounters undersaturated brine, sustaining a steep concentration gradient that drives a high dissolution flux and enhances local dissolution.

In addition, steep concentration gradients occur near the shale interfaces. This indicates that, although shale limits gas migration, brine enriched in dissolved CO_2 still diffuses into shale micropores. Over long periods, dissolution allows CO_2 to enter low-permeability media independently of capillary flow by transporting it as a solute into shale micropores, which increases the overall storage potential. Based on the normalized CO_2 concentration field in Figure 9, four grid points A(10,10), B(10,49), C(10,70) and D(10,82) are selected to examine the temporal evolution of dissolved CO_2 concentration.

Figure 10a shows a rapid increase in normalized CO_2 concentration at points A and B during the early injection period from day 0 to day 50. Both points lie in the near-well high-pressure zone, where rapid gas invasion increases gas saturation and interfacial areas. Dissolution increases and concentrations approach equilibrium rapidly. Thereafter, normalized CO_2 concentration at point B remains higher than at point A because B is adjacent to the lower interface of a lenticular shale layer, where gas accumulates and

sustains gas–brine contact, enhancing local dissolution mass transfer. At point A, migration pathways are less confined and fluids exchange continuously, which limits long-term gas residence and keeps normalized CO_2 concentration at a lower level.

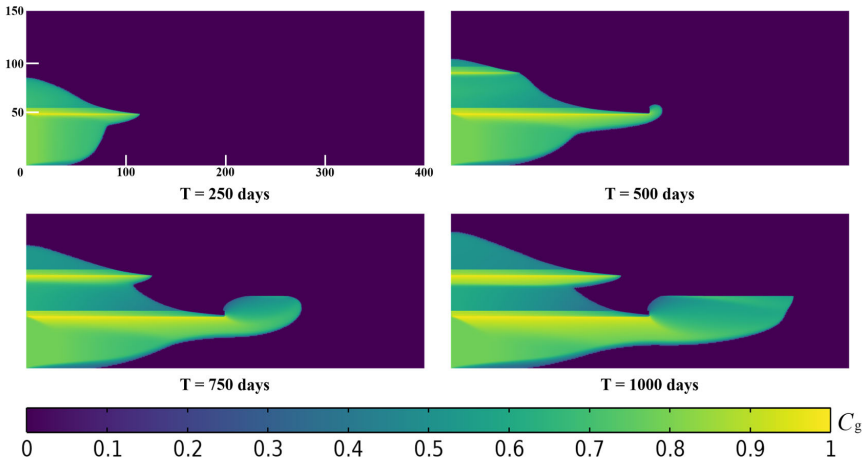


Figure 9. Temporal evolution of normalized CO_2 concentration in the saline aquifer during continuous CO_2 injection from 250 to 1000 days.

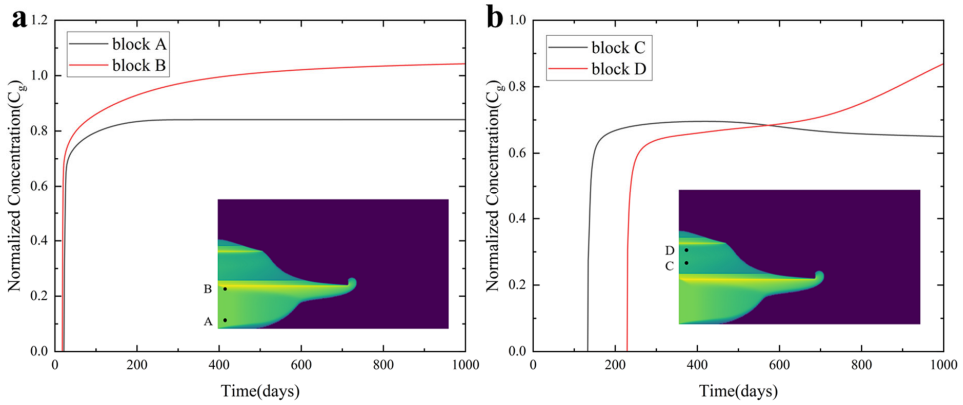


Figure 10. Evolution of normalized CO_2 concentration at the characteristic points over time (**a**) A(10,10), B(10,49) and (**b**) C(10,70), D(10,82).

Figure 10b shows the temporal evolution of normalized CO_2 concentration at two locations in the middle saline aquifer. Early in time, normalized CO_2 concentration increases faster at point C than at point D because of their position along the migration pathway. Point C lies in the lower part of the middle saline aquifer and sits on the main pathway of the upward flow supplied from below. Under buoyancy, the CO_2 plume passes point C before rising to point D, so point C encounters the gas source earlier, and dissolution begins there first. The curves cross at about day 580. After that time, normalized CO_2 concentration at point D continues to rise and exceeds point C, whereas point C shows a modest decline after reaching its peak and then remains lower. Point D is near the base of lenticular shale layer 3. When CO_2 reaches this depth, the shale limits upward flux and promotes secondary accumulation beneath the layer. Brine at point D remains in contact with CO_2 and continues mass transfer, which drives a sustained increase in dissolved concentration. In contrast, point C lies in the ascent pathway. As gas rises and accumulates near the aquifer top, gas-phase saturation along the flow path past point C decreases.

Overall, the lenticular shale layers promote gas accumulation beneath the layers, which increases residence time for gas–brine mass transfer. This heterogeneous architecture redirects migration from vertical ascent to lateral spreading and expands the

contact area between the plume and undersaturated brine, which increases dissolution trapping efficiency.

4.4. Effects of Permeability Anisotropy on CO_2 Dissolution

Figure 11 shows the spatiotemporal evolution of normalized CO_2 concentration in the reservoir matrix for four permeability anisotropy ratios. In subsurface reservoirs, horizontal and vertical matrix permeabilities may differ by orders of magnitude, which changes the balance between buoyant rise and lateral pressure-driven spreading. We define the permeability anisotropy ratio Γ as the ratio of vertical to horizontal permeability:

$$\Gamma = \frac{k_v}{k_h} \tag{21}$$

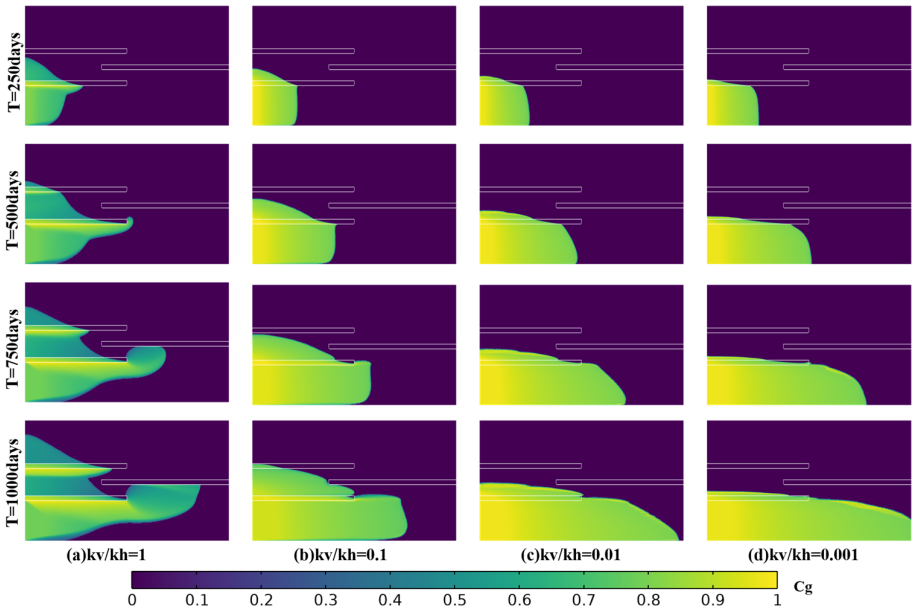


Figure 11. Spatiotemporal evolution of normalized CO_2 concentration from 250 to 1000 days under different permeability anisotropy ratios: (**a**) kv/kh = 1; (**b**) kv/kh = 0.1; (**c**) kv/kh = 0.01; and (**d**) kv/kh = 0.001. The white boxes highlight the lenticular shale layers in the model.

Here, k_v is the vertical permeability of the reservoir matrix, and k_h is the horizontal permeability of the reservoir matrix. Figure 11a shows that, under isotropic conditions, migration is dominated by vertical flow, and the high-concentration region exhibits pronounced vertical penetration. From day 500 to day 1000, high-concentration CO_2 does not accumulate extensively in the basal aquifer. Instead, it crosses the lenticular shale layer, migrates upward with time, and accumulates beneath the second lenticular shale layer.

Comparing Figure 11b,c shows that the high-concentration retention layer beneath the lenticular shale thickens as Γ decreases. Although CO_2 still crosses the lenticular shale, concentrations decrease after upward migration, indicating that part of the CO_2 is retained in the lower aquifers during transport. This behavior indicates that heterogeneity dilutes and delays the upward transfer of high CO_2 concentrations. When Γ equals 0.001, Figure 11d shows migration dominated by lateral spreading, with the high-concentration region confined beneath lenticular shale layer 1. Low vertical permeability increases resistance to upward flow and directs both fluid migration and pressure propagation toward the radial direction. The high-concentration layer remains continuous with a nearly uniform thickness and advances laterally in a piston-like manner. Relative to Figure 11a, the much lower vertical permeability suppresses vertical mixing and limits upward transport, so most injected CO_2 remains trapped at depth with high saturation.

Quantitatively, the storage efficiency factor decreases only from 0.294 to 0.291 as the permeability anisotropy ratio increases from 0.001 to 1. This small change indicates that the effect of anisotropy on storage efficiency remains limited, even across three orders of magnitude.

4.5. Effects of Injection Rate on CO_2 Dissolution

Figure 12 shows the evolution of normalized CO_2 concentration from day 250 to day 1000. At low injection rates, buoyancy controls migration as shown in Figure 12a. At day 1000, CO_2 migrates primarily upward, and the main gas body accumulated beneath lenticular shale layer 1 exhibits the shortest lateral extent. At low injection rates, viscous pressure gradients are small, and CO_2 does not overcome capillary pressure to drive extensive lateral displacement. Instead, buoyancy favors migration along vertical pathways.

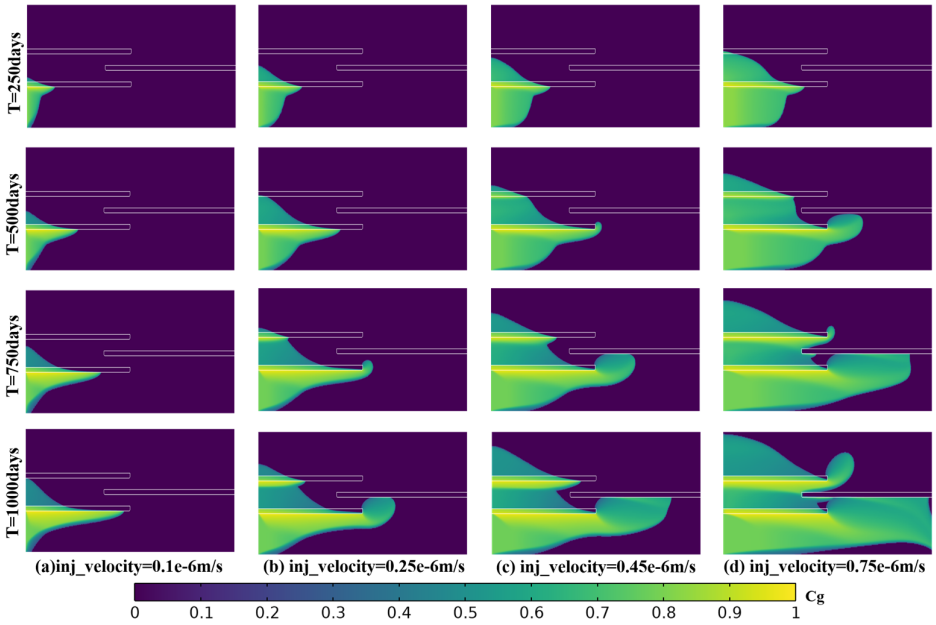


Figure 12. Spatiotemporal evolution of normalized CO_2 concentration from 250 to 1000 days at different injection rates: (**a**) inj_velocity = 0.1 × 10^{-6} m/s; (**b**) inj_velocity = 0.25 × 10^{-6} m/s; (**c**) inj_velocity = 0.45 × 10^{-6} m/s; and (**d**) inj_velocity = 0.75 × 10^{-6} m/s. The white boxes highlight the lenticular shale layers in the model.

In Figure 12d, the plume transitions toward a pressure-driven regime as injection rate increases. The basal high-concentration zone thickens and expands laterally beneath the shale, indicating stronger viscous forcing and a longer reach of the pressure perturbation. In the highest-rate case, the CO_2 front propagates across a larger radial distance by day 1000 to approach the domain boundary, and the stacked structure beneath successive shale layers becomes more pronounced. The lenticular shale layers still impose local accumulation due to high capillary entry pressure, but the larger imposed pressure gradient promotes earlier edge bypass and faster replenishment of upper-layer accumulations.

The high-rate cases also show multi-lobed and tongue-like concentration patterns near shale edges at late times. These features reflect competition between lateral sweep beneath the barrier and focused upward leakage at discrete bypass locations. As the injection rate rises, higher pore pressure near the barrier edges increases cross-layer flow through the most conductive pathways and strengthens interlayer connectivity of the plume. This rate dependence implies a tradeoff between lateral footprint and vertical migration risk and provides a mechanistic basis for linking operational rate to plume morphology and the spatial distribution of dissolution opportunity [54].

Quantitatively, the storage efficiency factor increases from 0.142 to 0.410 as the injection velocity rises from 0.1×10^{-6} m/s to 0.75×10^{-6} m/s. Within the investigated range, injection velocity has the strongest effect on storage efficiency.

4.6. Influence of Lenticular Shale Layer Geometry on CO_2 Dissolution Characteristics

This section evaluates how geometric parameters of lenticular shale layers control CO_2 plume evolution and storage security. We designed two sets of cases to isolate the effects of shale vertical thickness and radial length, with a simulation duration of 1000 days for all cases. Figure 13 shows simulations with a fixed shale radial length and shale vertical thicknesses of 6 m, 8 m, and 10 m. The three cases show that the large-scale migration pathway of the high-concentration plume remains similar from day 250 to day 1000. In all cases, CO_2 rises from the injection side, accumulates beneath the shale, and then bypasses at the shale edge to supply the overlying unit. Because changing thickness does not alter the radial location of the shale edge, the plume must traverse almost the same lateral distance beneath the barrier before an upward pathway develops, which explains the weak sensitivity of the macroscopic concentration field to thickness.

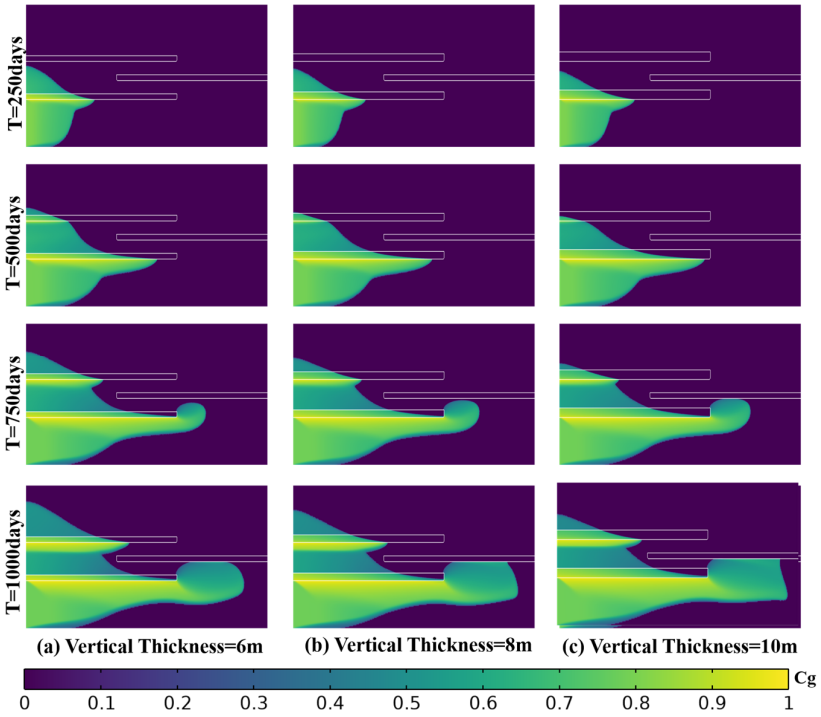


Figure 13. Spatiotemporal evolution of normalized CO_2 concentration from 250 to 1000 days under different vertical thicknesses of the lenticular shale layers: (**a**) vertical thickness = 6 m; (**b**) vertical thickness = 8 m; and (**c**) vertical thickness = 10 m. The white boxes highlight the lenticular shale layers in the model.

Although the overall pathway is consistent, shale thickness modifies the local structure of the accumulation beneath the barrier. In the thinnest shale case, the high-concentration tongue beneath the shale becomes established earlier, and the onset of edge bypass appears sooner, which yields a more elongated along-interface band at intermediate times. As thickness increases, CO_2 must build a larger local saturation and pressure anomaly beneath the shale before bypass initiates. This requirement shifts the basal accumulation from a more rounded front to a more boundary-aligned, quasi-rectangular pool with a thicker high-concentration core.

These differences indicate that shale thickness acts as a local control on the timing and sharpness of bypass rather than a primary control on plume reach. Over the simulated

period, thickness changes influence where high concentrations persist beneath the shale, but they do not strongly change how far the plume migrates laterally or how the upper accumulation develops once bypass has begun.

Figure 14 shows how the radial length of the lenticular shale controls plume evolution under otherwise identical conditions. Increasing shale length increases the lateral distance that CO_2 must travel beneath the barrier before reaching an edge, and increase residence time of high-concentration CO_2 in the lower unit and delay the formation of an upward bypass pathway. This geometric control is evident across the time sequence, where the shortest shale case exhibits early edge bypass and a boundary-attached upward finger, while the longer shale cases retain a larger fraction of the high-concentration core beneath the shale for a longer period.

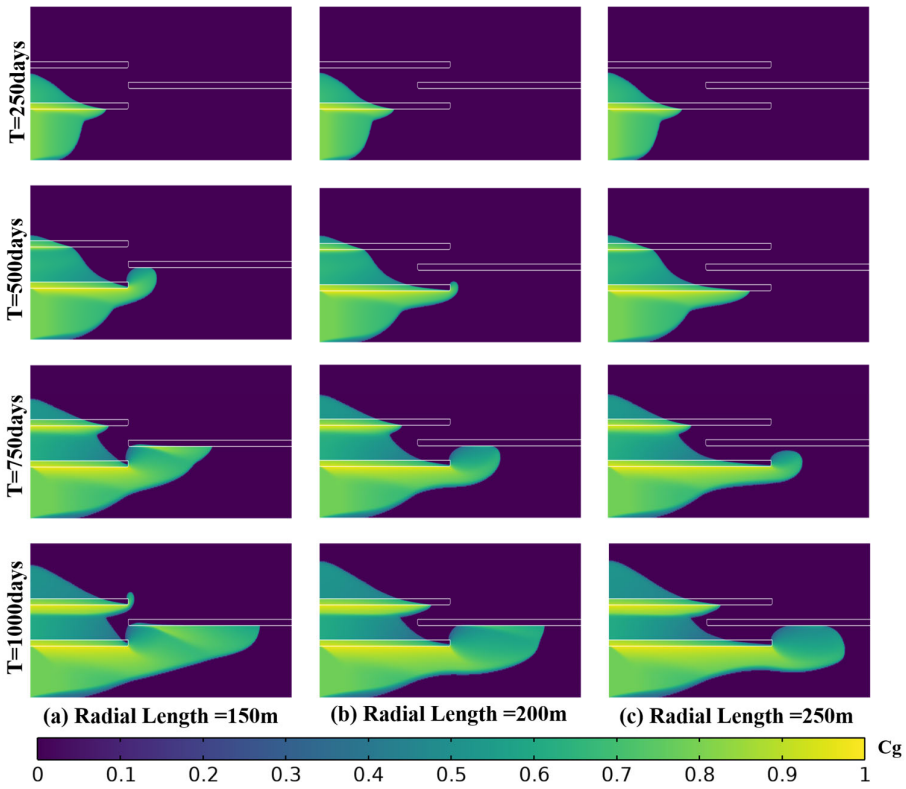


Figure 14. Spatiotemporal evolution of normalized CO_2 concentration from 250 to 1000 days under different radial lengths of the lenticular shale layers: (**a**) radial length = 150 m; (**b**) radial length = 200 m; and (**c**) radial length = 250 m. The white boxes highlight the lenticular shale layers in the model.

In the short-shale scenario, the plume rapidly reaches the barrier's edge, where buoyancy forces a swift upward bypass. This rapid vertical migration feeds the overlying layer, creating an elongated, high-concentration zone right next to the shale edge. As shale length increases, the upward finger weakens and the lower-layer accumulation expands. Continued injection mainly increases the volume of the basal pool beneath the shale to yield a more compact quasi-hemispherical retention zone that grows laterally and thickens over time.

By day 1000, the short-shale case shows a more extensive retention zone beneath the second shale due to earlier bypass, whereas the long-shale cases retain most CO_2 beneath the first barrier to demonstrate sustained storage at depth. These results indicate that shale length is a first-order geometric lever that regulates pathway tortuosity, controls the timing of vertical escape, and redistributes high concentrations between lower and upper aquifers.

Quantitatively, the storage efficiency factor increases from 0.289 to 0.292 as the shale radial length increases from 150 m to 250 m. It then rises from 0.292 to 0.295 as the shale

thickness increases from 6 m to 10 m. These results indicate that shale geometry promotes storage efficiency, but the overall effect remains limited.

4.7. Storage Efficiency Factor and a Nonlinear Multi-Parameter Power-Law Correlation Model

Based on the previously defined storage efficiency factor and the analyses of different controlling factors in Sections 4.4–4.6, a multi-parameter correlation model for the storage efficiency factor is further developed in this section. To represent the dominant mechanisms and eliminate dimensional effects, the relevant independent variables are further reformulated into dimensionless forms. We use a macroscopic capillary number *Ca** to represent the competition between viscous pressure gradients and the capillary threshold pressure:

$$Ca^* = \frac{\mu_{co_2} u_{inj} L}{k P_{ec}} \tag{22}$$

Here, μ_{CO2} is the dynamic viscosity of CO_2 (Pa·s), k is the matrix permeability (mD), and L is a characteristic length scale for fluid migration (m). Using the total reservoir thickness H_{res} as the characteristic length, we define the normalized shale radial length W_D and normalized shale thickness H_D as:

$$W_D = \frac{W}{H_{res}} \tag{23}$$

$$H_D = \frac{H}{H_{res}} \tag{24}$$

The recast dimensionless multi-parameter nonlinear power-law model is:

$$\epsilon = \kappa \cdot (Ca^*)^{\alpha} \cdot W_D^{\beta} \cdot H_D^{\gamma} \cdot \Gamma^{\delta} \tag{25}$$

Because geologic and engineering controls couple nonlinearly to influence storage efficiency, direct nonlinear fitting may lead to convergence difficulties and nonunique solutions. A logarithmic transformation is applied to convert the multiplicative nonlinear relationship into an additive linear form and then fit a multiple linear regression model:

$$\ln(\epsilon) = \ln(\kappa) + \alpha \ln(Ca^*) + \beta \ln(W_D) + \gamma \ln(H_D) + \delta \ln(\Gamma) \tag{26}$$

Then the equation can be written in the standard multiple linear form:

$$Y = \beta_0 + \sum \beta_i X_i \tag{27}$$

Here, $ln(\epsilon)$ is the response variable, and ln(*Ca**), ln(W_D), ln(H_D), and ln(Γ) are predictors. We fit the regression using ordinary least squares on the simulation dataset by minimizing the sum of squared residuals between observed and predicted log values, which yields unbiased parameter estimates with minimum variance under standard assumptions. We evaluate model performance using the coefficient of determination R^2 for goodness of fit and the root mean square error RMSE for predictive accuracy.

Regression on the simulation dataset shows good model fit, with R^2 greater than 0.92.

$$\epsilon = 0.073 \cdot (Ca^*)^{0.543} \cdot W_D^{0.020} \cdot H_D^{0.020} \cdot \Gamma^{-0.003} \tag{28}$$

In the dimensionless storage efficiency correlation shown in Figure 15, the constant 0.073 represents the characteristic storage coefficient for this geologic configuration. The exponents in the correlation reflect competition among the controlling mechanisms during CO_2 storage in deep saline aquifers. Storage efficiency ϵ increases with *Ca** following a

power law with an exponent of 0.543. Higher *Ca** indicates that viscous pressure gradients become more important relative to capillary thresholds. Once *Ca** exceeds a threshold, the macroscopic pressure drop can overcome capillary entry pressures in small pore throats. The exponent 0.543 indicates nonlinear gain. Increasing injection velocity increases both injected mass and reservoir pressure and promotes access to low-permeability pore space that would otherwise remain poorly connected.

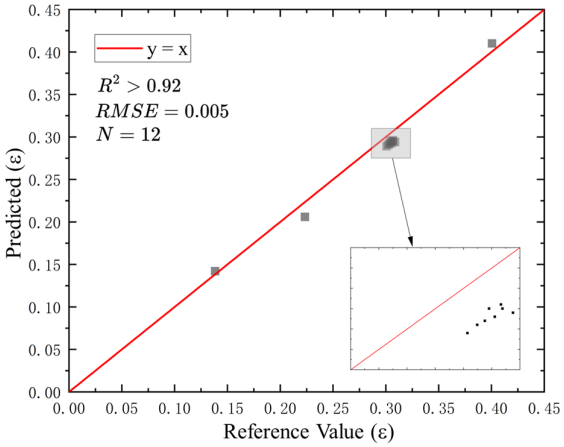


Figure 15. Dimensionless sequestration efficiency correlation.

In addition, the exponents for the normalized shale radial length W_D and normalized shale thickness H_D are both 0.020, indicating a robust positive association between lenticular shale geometry and storage efficiency. The mechanism is that shale layers act as physical baffles that increase pathway tortuosity and gas-brine contact time, which promotes residual gas trapping. The exponent for the permeability anisotropy ratio is −0.003, indicating a weak suppressing effect. This suggests that, in this heterogeneous setting, although Γ influences vertical migration in homogeneous media, flow steering by the lenticular geometry dominates the flow field and reduces the macroscopic contribution of anisotropy to storage efficiency. From an engineering perspective, this dimensionless correlation offers a practical basis for evaluating storage performance. The macroscopic capillary number *Ca** is a key indicator for optimizing injection velocities. The geometric parameters W_D and H_D provide quantitative metrics for site selection. The permeability anisotropy ratio Γ has a limited quantitative effect under the investigated heterogeneous conditions. Even so, it remains relevant for characterizing the tendency for vertical flow.

4.8. Sensitivity Analysis of the Storage Efficiency Factor to Key Parameters

Figure 16 shows the sensitivity of the storage efficiency factor to *Ca**, W_D, H_D, and Γ. Among these parameters, *Ca** has the strongest effect on the storage efficiency factor ϵ. As *Ca** increases, ϵ rises from 0.142 to 0.410 and shows a clear nonlinear increase. This trend suggests that stronger viscous forces under higher injection conditions improve the ability of CO_2 to enter and occupy the pore space, which increases storage efficiency. This result agrees with the dimensionless correlation analysis in Section 4.7 and confirms that *Ca** is the dominant parameter controlling ϵ.

By contrast, increases in W_D and H_D produce only small increases in ϵ, whereas changes in Γ cause little variation in ϵ. This result indicates that the geometric scale of the shale layers has a positive but limited effect on storage efficiency. Permeability anisotropy is also not a primary control on macroscopic storage efficiency within the investigated range. Overall, the sensitivity analysis shows that the relative influence of the investigated parameters on storage efficiency follows the order $Ca^* > W_D \approx H_D > \Gamma$.

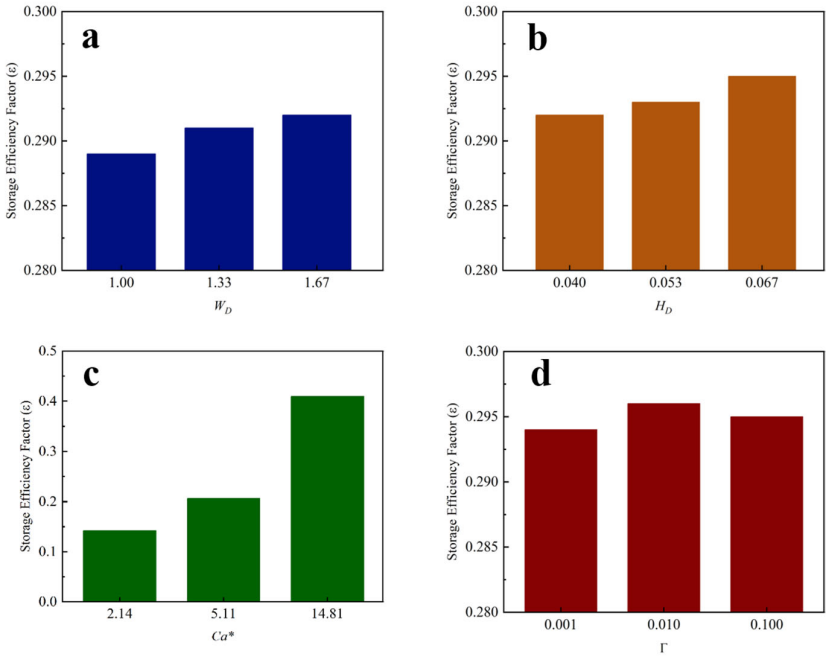


Figure 16. Sensitivity analysis of the storage efficiency factor ϵ to key parameters: (**a**) lenticular radial length W_D; (**b**) shale thickness H_D; (**c**) injection velocity Ca^*; and (**d**) permeability anisotropy ratio Γ.

4.9. Qualitative Discussion on Long-Term Geochemical Effects and Future Outlook

The current numerical simulations focus on multiphase flow and dissolution processes over short to medium timescales. However, geochemical interactions between CO_2, brine, and minerals influence long-term storage security in deep saline aquifers [55]. Over long time scales, lenticular shale layers may influence the spatial distribution of reaction zones and the progression of the chemical weathering front by modifying the residence time and migration pathways of CO_2-rich brine. Low-permeability barriers promote lateral plume spreading beneath the barrier before upward migration resumes [56], which implies that CO_2-rich, low-pH brine may persist and spread along the underside of lenticular layers. As a result, the chemical weathering front is expected to extend preferentially along the shale base rather than remaining confined to a near-well vertical pathway.

On a long-term scale, these fluid stagnation regions at the shale bottom and the bypass channels at the edges may evolve into concentrated geochemical reaction zones. Within these local reaction bands, prolonged fluid-rock interactions initially drive the dissolution of primary minerals such as feldspar or carbonate cements, leading to a slight increase in local porosity [57]. As the reactions proceed, the precipitation of secondary carbonate minerals becomes dominant. This dissolution-and-precipitation process in localized areas induces heterogeneous changes in reservoir porosity and permeability. Long-term secondary mineral precipitation may clog the micro pore throats of the bypass channels at the edges of the lenses, causing a further reduction in local permeability [58]. From a long-term perspective, such heterogeneous changes in physical properties induced by local concentrated reactions reinforce the physical sealing capacity of the lenticular formations, improving the overall safety of CO_2 sequestration.

The computational framework of this study does not include quantitative simulations of the complex mineral dissolution and precipitation processes mentioned above. Future work may introduce coupled thermal, hydrological, mechanical, and chemical models. Such models would provide an in-depth quantitative assessment of the heterogeneous evolution mechanisms of porosity and permeability along with the long-term distribution of reaction zones under the constraints of heterogeneous lenses.

5. Conclusions

In this study, a two-dimensional coupled-process numerical model was developed to investigate how discontinuous lenticular shale layers influence CO_2 migration and dissolution in a saline formation. Sensitivity analyses of permeability anisotropy, injection rate, and lenticular shale geometry, together with dimensionless analysis, support the following conclusions:

(1) Lenticular shale layers form local capillary barriers that limit vertical escape of CO_2 and increase dissolution trapping potential. The discontinuous shale architecture forces a tortuous pathway that includes lateral spreading, bypass flow around shale termini, and renewed spreading above. This pathway delays early breakthrough and promotes sweep of the upper portions of the saline aquifer, which increases gas–brine interfacial area and mass-transfer time and enhances dissolution trapping.

(2) Decreasing the permeability anisotropy ratio Γ strengthens shielding by the lenticular shale layers. When Γ equals 0.001, the flow field becomes laterally dominated and the gas phase remains largely confined beneath the shale. As Ca^* increases, viscous pressure gradients overcome capillary threshold pressures, which expands lateral plume extent and produces multilayer tongue-like advance. Among the geometric controls, increasing shale radial length increases pathway tortuosity and deep residence time, whereas shale thickness has a weaker effect.

(3) Using simulation data and dimensional analysis, we propose a nonlinear power-law model in terms of Ca^*, lenticular shale geometry, and permeability anisotropy. The model indicates that storage efficiency is controlled jointly by viscous forcing and structural constraints in a heterogeneous reservoir. The resulting dimensionless correlation shows that higher injection rates increase access to low-permeability pore space and that lenticular shale layers contribute additional retention space.

Overall, evaluating CO_2 storage potential requires accounting for the spatial distribution of discontinuous lenticular shale layers within the reservoir. These results refine understanding of multiphase migration under complex geologic conditions and provide guidance for injection well placement and operational parameter design.

Author Contributions: Conceptualization, B.W.; Methodology, B.W. and J.Y.; Formal analysis, J.Y.; Investigation, Y.T. and J.S.; Validation, J.S.; Resources, C.C.; Data curation, K.F.; Writing—original draft preparation, B.W. and Y.T.; Writing—review & editing, C.C. and S.L.; Visualization, Y.B.; Supervision, C.C. and S.L.; Funding acquisition, B.W. and C.C. All authors have read and agreed to the published version of the manuscript.

Funding: This study was supported by the National Natural Science Foundation of China (No. 52306187); the Fundamental Research Funds for the Central Universities of China (Grant No. 3132024205 and 3132023527), the China Scholarship Council (No. 201703780060), and the Open Fund of the Key Laboratory of Ocean Energy Utilization and Energy Conservation of Ministry of Education (Grant No. LOEC-202004).

Data Availability Statement: The original contributions presented in this study are included in the article. Further inquiries can be directed to the corresponding author.

Conflicts of Interest: The authors declare no conflicts of interest.

References

1. Mert, E.; Aksu, M.; Celiktas, M.S. Projections of Global Energy Transition Models in the Wake of Industrial Revolution and Climate Change Policies. *Clean Energy Sci. Technol.* **2025**, *3*, 273–301. [CrossRef]
2. Michaelides, E.E. Power and Energy Requirements for Carbon Capture and Sequestration. *Thermo* **2025**, *5*, 8. [CrossRef]
3. Gidden, M.J.; Joshi, S.; Armitage, J.J.; Christ, A.-B.; Boettcher, M.; Brutschin, E.; Köberle, A.C.; Riahi, K.; Schellnhuber, H.J.; Schleussner, C.-F.; et al. A Prudent Planetary Limit for Geologic Carbon Storage. *Nature* **2025**, *645*, 124–132. [CrossRef] [PubMed]

4. Bachu, S. CO_2 Storage in Geological Media: Role, Means, Status and Barriers to Deployment. *Prog. Energy Combust. Sci.* **2008**, *34*, 254–273. [CrossRef]
5. Rutqvist, J. The Geomechanics of CO_2 Storage in Deep Sedimentary Formations. *Geotech. Geol. Eng.* **2012**, *30*, 525–551. [CrossRef]
6. Kelemen, P.; Benson, S.M.; Pilorgé, H.; Psarras, P.; Wilcox, J. An Overview of the Status and Challenges of CO_2 Storage in Minerals and Geological Formations. *Front. Clim.* **2019**, *1*, 9. [CrossRef]
7. Shen, J.; Mo, F.; Tao, Z.; Hong, Y.; Gao, B.; Xuan, T. Numerical Investigation of Offshore CCUS in Deep Saline Aquifers Using Multi-Layer Injection Method: A Case Study of the Enping 15-1 Oilfield CO_2 Storage Project, China. *J. Mar. Sci. Eng.* **2025**, *13*, 1247. [CrossRef]
8. Vivek, R.; Kumar, G.S. Numerical Investigation on Effect of Varying Injection Scenario and Relative Permeability Hysteresis on CO_2 Dissolution in Saline Aquifer. *Environ. Earth Sci.* **2016**, *75*, 1192. [CrossRef]
9. Ding, T.; Liu, Y.; Hua, X. Influence of Interphase Mass Transfer and Diffusion Processes on CO_2-Brine Displacement in Saline Aquifers. *Environ. Earth Sci.* **2019**, *78*, 654–669. [CrossRef]
10. Alshakri, J.; Hampson, G.; Jacquemyn, C.; Jackson, M.; Petrovskyy, D.; Geiger, S.; Silva, J.D.M.; Judice, S.; Rahman, F.; Sousa, M.C. A Screening Assessment of the Impact of Sedimentological Heterogeneity on CO_2 Migration and Stratigraphic-Baffling Potential: Sherwood and Bunter Sandstones, UK. *Geol. Soc. Spec. Publ.* **2023**, *528*, 245–266. [CrossRef]
11. Jackson, W.A.; Hampson, G.J.; Jacquemyn, C.; Jackson, M.D.; Petrovskyy, D.; Geiger, S.; Machado Silva, J.D.; Judice, S.; Rahman, F.; Costa Sousa, M. A Screening Assessment of the Impact of Sedimentological Heterogeneity on CO_2 Migration and Stratigraphic-Baffling Potential: Johansen and Cook Formations, Northern Lights Project, Offshore Norway. *Int. J. Greenh. Gas Control* **2022**, *120*, 103762. [CrossRef]
12. Bakhshian, S.; Bump, A.P.; Pandey, S.; Ni, H.; Hovorka, S.D. Assessing the Potential of Composite Confining Systems for Secure and Long-Term CO_2 Retention in Geosequestration. *Sci. Rep.* **2023**, *13*, 21022. [CrossRef] [PubMed]
13. Li, Z.; Xu, T.; Tian, H.; Pan, R. The Impacts of Reservoir Heterogeneities on the CO_2-Enhanced Oil Recovery Process—A Case Study of Daqingzijing Block in Jilin Oilfield, China. *Energies* **2024**, *17*, 6128. [CrossRef]
14. Hansen, S.K.; Tao, Y.; Karra, S. Impacts of Permeability Heterogeneity and Background Flow on Supercritical CO_2 Dissolution in the Deep Subsurface. *Water Resour. Res.* **2023**, *59*, e2023WR035394. [CrossRef]
15. Fang, X.; Lv, Y.; Yuan, C.; Zhu, X.; Guo, J.; Liu, W.; Li, H. Effects of Reservoir Heterogeneity on CO_2 Dissolution Efficiency in Randomly Multilayered Formations. *Energies* **2023**, *16*, 5219. [CrossRef]
16. Shi, Z.; Qin, J.; Xu, N.; Qin, Y.; Zhang, B.; Feng, S.; Chen, L.; Wang, H. A Multi-Factor Comparative Study on H2 and CO_2 Migration Behaviors in Saline Aquifers. *Appl. Sci.* **2025**, *15*, 13107. [CrossRef]
17. Cavanagh, A.J.; Haszeldine, R.S. The Sleipner Storage Site: Capillary Flow Modeling of a Layered CO_2 Plume Requires Fractured Shale Barriers within the Utsira Formation. *Int. J. Greenh. Gas Control* **2014**, *21*, 101–112. [CrossRef]
18. Wen, G.; Benson, S.M. CO_2 Plume Migration and Dissolution in Layered Reservoirs. *Int. J. Greenh. Gas Control* **2019**, *87*, 66–79. [CrossRef]
19. Furre, A.-K.; Warchoł, M.J.; Alnes, H.; Pontén, A.S.M. Sleipner 26 Years: How Well-Established Subsurface Monitoring Work Processes Have Contributed to Successful Offshore CO_2 Injection. *Geoenergy* **2024**, *2*, geoenergy2024-015. [CrossRef]
20. Hawez, H.K.; Asim, T. Impact of Regional Pressure Dissipation on Carbon Capture and Storage Projects: A Comprehensive Review. *Energies* **2024**, *17*, 1889. [CrossRef]
21. Mortimer, P.K.; Mingotti, N.; Woods, A.W. A Dynamic Model of CO_2 Storage in Layered Anticlines. *J. Fluid Mech.* **2024**, *979*, A39. [CrossRef]
22. Ni, H.; Li, B.; Darraj, N.; Ren, B.; Harris, C.; Krishnamurthy, P.G.; Bukar, I.; Berg, S.; Snippe, J.; Ringrose, P.; et al. The Impact of Capillary Heterogeneity on CO_2 Flow and Trapping across Scales. *Earth-Sci. Rev.* **2025**, *270*, 105257. [CrossRef]
23. Abbaszadeh, M.; Shariatipour, S.M. Investigating the Impact of Reservoir Properties and Injection Parameters on Carbon Dioxide Dissolution in Saline Aquifers. *Fluids* **2018**, *3*, 76. [CrossRef]
24. Wang, Y.; Fernàndez-Garcia, D.; Saaltink, M.W. Numerical Analysis of the Effect of Heterogeneity on CO_2 Dissolution Enhanced by Gravity-Driven Convection. *Hydrol. Earth Syst. Sci.* **2025**, *29*, 2485–2503. [CrossRef]
25. Callioli Santi, A.; Ringrose, P.; Eidsvik, J.; Haugdahl, T.A. Invasion Percolation Markov Chains—A Probabilistic Framework for Assessing Vertical CO_2 Migration. *Int. J. Greenh. Gas Control* **2025**, *142*, 104338. [CrossRef]
26. Andersen, O.; Gasda, S.E.; Nilsen, H.M. Vertically Averaged Equations with Variable Density for CO_2 Flow in Porous Media. *Transp. Porous Media* **2015**, *107*, 95–127. [CrossRef]
27. Cheng, M.; Guo, H.; Cao, F.; Gong, J.; Du, F. Integrated Experimental and Numerical Analysis of Particle Migration Effects on Produced Water Reinjection in Offshore Reservoirs. *Fluid Dyn. Mater. Process.* **2025**, *21*, 2629–2650. [CrossRef]
28. Brooks, R.H. *Hydraulic Properties of Porous Media*; Colorado State University: Fort Collins, CO, USA, 1964.
29. Pini, R.; Benson, S.M. Simultaneous Determination of Capillary Pressure and Relative Permeability Curves from Core-Flooding Experiments with Various Fluid Pairs. *Water Resour. Res.* **2013**, *49*, 3516–3530. [CrossRef]

30. Oak, M.J.; Baker, L.E.; Thomas, D.C. Three-Phase Relative Permeability of Berea Sandstone. *J. Pet. Technol.* **1990**, *42*, 1054–1061. [CrossRef]
31. Krevor, S.C.M.; Pini, R.; Zuo, L.; Benson, S.M. Relative Permeability and Trapping of CO_2 and Water in Sandstone Rocks at Reservoir Conditions. *Water Resour. Res.* **2012**, *48*, W02532. [CrossRef]
32. Gudala, M.; Govindarajan, S.K.; Yan, B.; Sun, S. Comparison of Supercritical CO_2 with Water as Geofluid in Geothermal Reservoirs with Numerical Investigation Using Fully Coupled Thermo-Hydro-Geomechanical Model. *J. Energy Resour. Technol.* **2023**, *145*, 61302. [CrossRef]
33. Buckley, S.E.; Leverett, M.C. Mechanism of Fluid Displacement in Sands. *Trans. AIME* **1942**, *146*, 107–116. [CrossRef]
34. Nugraha, M.G.; Andersson, R.; Andersson, B. On the Sherwood Number Correction Due to Stefan Flow. *Chem. Eng. Sci.* **2022**, *249*, 117292. [CrossRef]
35. Niessner, J.; Hassanizadeh, S.M. Non-Equilibrium Interphase Heat and Mass Transfer during Two-Phase Flow in Porous Media—Theoretical Considerations and Modeling. *Adv. Water Resour.* **2009**, *32*, 1756–1766. [CrossRef]
36. Gray, W.G.; Miller, C.T. Thermodynamically Constrained Averaging Theory Approach for Modeling Flow and Transport Phenomena in Porous Medium Systems: 1. Motivation and Overview. *Adv. Water Resour.* **2005**, *28*, 161–180. [CrossRef]
37. Wang, S.; Tian, H.; Zhao, X.; Yan, Y.; Yang, X.; Wang, X. Assessment of the Geological Storage Potential and Suitability of CO_2 in the Deep Saline Aquifers in the Northwest Plain of Shandong Province, China. *Energies* **2024**, *17*, 6387. [CrossRef]
38. Liu, H.; Zhang, S.; Song, G.; Xuejun, W.; Teng, J.; Wang, M.; Bao, Y.; Yao, S.; Wang, W.; Zhang, S.; et al. Effect of Shale Diagenesis on Pores and Storage Capacity in the Paleogene Shahejie Formation, Dongying Depression, Bohai Bay Basin, East China. *Mar. Pet. Geol.* **2019**, *103*, 738–752. [CrossRef]
39. Chu, A.K.; Benson, S.M.; Wen, G. Deep-Learning-Based Flow Prediction for CO_2 Storage in Shale–Sandstone Formations. *Energies* **2023**, *16*, 246. [CrossRef]
40. Frykman, P.; Nielsen, C.M.; Dalhoff, F.; Sørensen, A.T.; Klinkby, L.; Nielsen, L.H. Geological Modelling for Site Evaluation at the Vedsted Structure, NW Denmark. *Energy Procedia* **2011**, *4*, 4711–4718. [CrossRef]
41. Shao, Q.; Boon, M.; Youssef, A.; Kurtev, K.; Benson, S.M.; Matthai, S.K. Modelling CO_2 Plume Spreading in Highly Heterogeneous Rocks with Anisotropic, Rate-Dependent Saturation Functions: A Field-Data Based Numeric Simulation Study of Otway. *Int. J. Greenh. Gas Control* **2022**, *119*, 103699. [CrossRef]
42. Hu, G.; Yi, X.; Tian, X.; Wang, R.; Li, P.; Peng, L.; Liang, X. Assessing CO_2 Storage Mechanisms in Marine Shallow Sediments to Mitigate Leakage Risks from Sub-Seabed Carbon Storage: A Numerical Simulation Study. *Front. Mar. Sci.* **2025**, *12*, 1547326. [CrossRef]
43. Kumar, A.; Ozah, R.; Noh, M.; Pope, G.A.; Bryant, S.; Sepehrnoori, K.; Lake, L.W. Reservoir Simulation of CO_2 Storage in Deep Saline Aquifers. *SPE J.* **2005**, *10*, 336–348. [CrossRef]
44. Ye, L.; Liu, Z.; Du, J.; Jia, C.; Zhu, H.; Liu, F. Geological Storage Test and Transport Rule of CO_2 in Saline Aquifers: A Case Study of Dezhou Carbon Storage Demonstration Zone in Shandong Province. *Fuel* **2024**, *377*, 132752. [CrossRef]
45. Liu, B.; Xu, J.; Li, Z.; Malekian, R.; Xu, Z. Modeling of CO_2 Transport and Pressure Buildup in Reservoirs during CO_2 Storage in Saline Aquifers: A Case in Dongying Depression in China. *Environ. Earth Sci.* **2018**, *77*, 158. [CrossRef]
46. Chen, Q.; Hou, J.; Wei, B.; Gong, R.; Du, Q.; Liu, Y. Study on CO_2 Storage Suitability Evaluation and Storage Potential Prediction Method in Site-Level Saline Aquifer: A Case Study of X Saline Aquifer Block in Enping 15-1 Oilfield. *Geoenergy Sci. Eng.* **2025**, *246*, 213598. [CrossRef]
47. Nazari, N.; Taylor, S.; Mostowfi, F. CO_2 Sequestration in Geological Formations: Insights into Mineral Reactions and Reservoir Dynamics. *Earth-Sci. Rev.* **2025**, *269*, 105200. [CrossRef]
48. Wu, B.; Zhang, X.; Liu, H.; Ji, Y. Numerical Modelling of CO_2 Plume Evolution and Dissolution in a Stratified Saline Aquifer. *Fluid Dyn. Mater. Process.* **2025**, *21*, 2359–2387. [CrossRef]
49. Jordan, P.; Doughty, C. Sensitivity of CO_2 Migration Estimation on Reservoir Temperature and Pressure Uncertainty. *Energy Procedia* **2009**, *1*, 2825–2832. [CrossRef]
50. Kumar, R.; Campbell, S.W.; Cunningham, J.A. Effect of Temperature on the Geological Sequestration of CO_2 in a Layered Carbonate Formation. *J. Energy Resour. Technol.* **2020**, *142*, 070907. [CrossRef]
51. He, F.; Tan, R.; Jiang, S.; Qian, C.; Bu, C.; Wang, B. Deep Learning-Based Investigation of Multiphase Flow and Heat Transfer in CO_2–Water Enhanced Geothermal Systems. *Fluid Dyn. Mater. Process.* **2025**, *21*, 2557–2577. [CrossRef]
52. Goodman, A.; Hakala, A.; Bromhal, G.; Deel, D.; Rodosta, T.; Frailey, S.; Small, M.; Allen, D.; Romanov, V.; Fazio, J.; et al. U.S. DOE Methodology for the Development of Geologic Storage Potential for Carbon Dioxide at the National and Regional Scale. *Int. J. Greenh. Gas Control* **2011**, *5*, 952–965. [CrossRef]
53. Bachu, S. Review of CO_2 Storage Efficiency in Deep Saline Aquifers. *Int. J. Greenh. Gas Control* **2015**, *40*, 188–202. [CrossRef]
54. Wang, W.; Zhao, Y.; Li, B.; Guan, B.; Sun, H.; Zhang, T. CO_2 Injection to Mitigate Reservoir Damage in Edge/Bottom-Water Condensate Gas Reservoirs. *Fluid Dyn. Mater. Process.* **2025**, *21*, 2331–2357. [CrossRef]

55. Kampman, N.; Busch, A.; Bertier, P.; Snippe, J.; Hangx, S.; Pipich, V.; Di, Z.; Rother, G.; Harrington, J.F.; Evans, J.P.; et al. Observational Evidence Confirms Modelling of the Long-Term Integrity of CO_2-Reservoir Caprocks. *Nat. Commun.* **2016**, *7*, 12268. [CrossRef]
56. Cossins, T.; Mishra, A.; Haese, R.R. The Feasibility of Enhanced Pore Space Utilization in CO_2 Storage Reservoirs Using an Artificially Emplaced Si-Gel Flow Barrier. *Sci. Rep.* **2023**, *13*, 9334. [CrossRef]
57. Xu, T.; Zheng, L.; Tian, H. Reactive Transport Modeling for CO_2 Geological Sequestration. *J. Pet. Sci. Eng.* **2011**, *78*, 765–777. [CrossRef]
58. Hou, L.; Yu, Z.; Luo, X.; Wu, S. Self-Sealing of Caprocks during CO_2 Geological Sequestration. *Energy* **2022**, *252*, 124064. [CrossRef]

Disclaimer/Publisher's Note: The statements, opinions and data contained in all publications are solely those of the individual author(s) and contributor(s) and not of MDPI and/or the editor(s). MDPI and/or the editor(s) disclaim responsibility for any injury to people or property resulting from any ideas, methods, instructions or products referred to in the content.